Materials Today Energy 53 (2025) 102029

Contents lists available at ScienceDirect

Materials Today Energy

journal homepage: www.journals.elsevier.com/materials-today-energy/

Small-molecule-based hole-transporting auxiliaries for efficient organic solar cells

Ji Youn Kim, Sung Jae Jeon, Nam Gyu Yang, Ye Chan Kim, Doo Kyung Moon *

Nano and Information Materials Laboratory, Department of Chemical Engineering, Konkuk University, 120 Neungdong-ro, Gwangjin-gu, Seoul, 05029, Republic of Korea

A R T I C L E I N F O

Keywords:
Organic solar cells
Semi-transparent organic solar cells
Stability
Universality
Interface engineering

A B S T R A C T

Organic solar cells (OSCs) are highly promising for their versatility in device engineering and active layer tuning, enabling applications such as semi-transparent solar cells. Herein, two small molecules, DTDCPB and DPDCPB, were introduced as hole-transporting auxiliaries (HTAs) onto PEDOT:PSS matrix to form bilayer hole transport layers (HTLs), enabling effective interfacial engineering through a straightforward fabrication process. Among them, DTDCPB effectively aligned energy levels with the active layer, enhanced charge transport and extraction, and improved conductivity, which assisted in suppressing charge recombination and validated interfacial engineering as an effective strategy for optimizing device performance. As a result, the DTDCPB based OSCs (Device 1 - D18/L8-BO) achieved enhanced power conversion efficiency of 17.54%, compared to 16.92% for the control device, along with improved operational stability. More importantly, Device 1, Device 2 (P(3IN = 0.3)(3IN2F = 0.5)(BDD = 0.2):BTP-eC9), and Device 3 (PTB7-Th:IEICO-4F) exhibited increased light use efficiencies (LUEs) of 2.91%, 3.94%, and 3.12%, respectively, which are higher than those of the corresponding control devices (2.84%, 3.72%, and 3.10%). This improvement is attributed not only to the universality of the HTA strategy but also to the enhanced average visible transmittance, highlighting the considerable potential of this approach for high-quality ST-OSCs.

1. Introduction

Organic solar cells (OSCs) have surpassed 20% power conversion efficiency (PCE), outperforming prior benchmarks owing to advances in materials and device engineering [1,2]. Interfacial engineering is key to achieving high-efficiency OSCs. The energy level mismatch and charge recombination occurring at the interface between the active and charge transport layers are major factors determining efficiency. Various material-based approaches and techniques have been developed to address these challenges [3,4].

Poly(3,4-ethylenedioxythiophene):poly(styrenesulfonate) (PEDOT:PSS) and molybdenum(VI) oxide (MoO_3) have been widely used as HTLs in conventional and inverted OSC architectures, respectively, yielding high photovoltaic performance. PEDOT:PSS is a water-based, solution-processable conducting polymer for OSCs [5,6]. In addition, PEDOT:PSS and MoO_3 facilitate hole transport by alleviating interfacial contact issues and enabling the energy levels to be tuned. However, the high acidity and hygroscopic nature of PSS compromise the ambient stability of the device, leading to the long-term corrosion of the indium tin oxide (ITO) electrode and resulting in substantial efficiency degradation [7–9].

Researchers are focusing on approaches involving the additional doping of PEDOT:PSS with other hole-transport materials through bilayer or hybrid techniques to overcome the inherent drawbacks of PEDOT:PSS and develop more efficient OSCs [5,10–12]. Chen et al. fabricated bilayer HTLs through incorporating DFTAB, a star-shaped benzene-based molecule, with PEDOT:PSS to increase interfacial stability. DFTAB facilitates charge transfer by modulating its peripheral amine groups and the electron-rich PEDOT:PSS architecture surrounding the electron-deficient core, resulting in suitable electron affinity for efficient hole transport. Casted onto the PEDOT:PSS layer promotes the required interfacial interactions with the active layer, thereby enhancing the crystallinity and facilitating efficient charge transport. As a result, the PCE was increased to 18.59% compared with that of the control device (18.01%). The DFTAB-modified device was substantially more photostable under continuous 1-sun illumination (270 h vs. 60 h), retaining 80% of the initial PCE (T_{80}). These results suggest that DFTAB acts as a UV-blocking layer that mitigates photo-induced degradation,

---

* Corresponding author.
E-mail address: dkmoon@konkuk.ac.kr (D.K. Moon).

https://doi.org/10.1016/j.mtener.2025.102029
Received 2 May 2025; Received in revised form 28 July 2025; Accepted 17 August 2025

highlighting its potential for the development of highly efficient and stable OSCs [3].

Chen et al. designed a hybrid HTL by blending PEDOT:PSS with highly conductive polypyrrole (PPy) and phosphomolybdic acid to form PPy7. This hybrid HTL enhanced the charge collection efficiency and suppressed charge recombination, resulting in a PCE of 18.2% compared with the 17.7% of the control device. Under continuous 1-sun illumination, the T_{80} of the hybrid HTL-based device reached 191 h, compared to 35 h for the control device, and thermal stability tests showed a similar trend after 29 h (89% vs. 80%), further highlighting its superior thermal durability [12].

Gao et al. constructed a hybrid HTL through doping PEDOT:PSS with an Fe_3O_4/graphene oxide (GO) magnetic nanocomposite. The incorporation of this nanocomposite promoted the phase separation between the PEDOT and PSS and expanded the PEDOT domains, increasing the conductivity. The target device exhibited a higher PCE than the control device (18.91% vs. 18.37%, respectively) due to the uniform distribution of the Fe_3O_4 nanoparticles across the GO surface. This effect demonstrates universal applicability in various active-layer systems: PM6:Y6 (control device PCE = 16.46%; target device PCE = 17.28%) and PBDB-T:ITIC (control device PCE = 9.68%; target device, PCE = 10.67%) [13].

Well-defined small-molecule materials are simple to process, highly reproducible, and suitable for large-scale fabrication. These materials have been widely used in OSC active layers owing to their charge transport properties [14,15]. In particular, triphenylamine (TPA)-based donor–acceptor–acceptor (D-A-A) architectures allow detailed energy level adjustments through the incorporation of two acceptor units, which increases intramolecular charge transfer (ICT), charge separation, and charge mobility [15,16]. Kan et al. introduced a hybrid HTL incorporating MPA2FPh-BT-BA (2F), a D-A-A-structured molecule, into a PEDOT:PSS matrix to overcome the thickness tolerance limitations of PEDOT:PSS. This approach increased charge extraction through altering the interfacial dipoles to modulate the work function (WF) and achieved a maximum PCE of 19.2% [17]. Therefore, such well-designed small-molecule materials hold great promise for diverse applications in advanced optoelectronic devices.

Recently, strategies for enhancing OSC performance using interfacial engineering auxiliaries (IEAs) have been actively reported. IEAs are materials or techniques introduced between material interfaces or adjacent layers to assist in interfacial engineering [18]. IEAs can diffuse or vanish after incorporation and be used to precisely regulate interfacial interactions, enabling the performance of OSCs to be altered [19]. Huang et al. introduced *n*-octane, which has low vapor pressure and an appropriate diffusion coefficient, as an ecofriendly solvent protection (ESP) layer to a donor film and developed an efficient and reproducible sequential deposition (SD) process. The acceptor solution was prepared in the same host solvent as the donor solution and introduced; the underlying film remained intact and contributed to the formation of a uniform interface. This process suppressed interfacial charge recombination and increased phase compatibility, yielding a higher PCE than the control device (17.52% vs. 15.32%, respectively). This method is an effective IEA strategy for fabricating highly efficient and reproducible OSCs [20]. Yan et al. followed a similar approach used in prior studies to introduce a dithieno[3,2-b:2′,3′-d]thiophene (DTT) solid additive onto a D18-Cl layer to fabricate efficient SD-based OSCs. The presence of DTT in the D18-Cl layer facilitated the formation of a highly crystalline fibrous network and induced a nanoporous morphology, which together suppressed charge recombination and enhanced charge transport, ultimately resulting in a higher PCE (19.04% vs. 18.03%). The study demonstrated the potential of IEA-based active layer engineering for the development of environmentally friendly and high-efficiency OSCs [18].

Bao et al. introduced a ferroelectric polymer PVDF-TrFE between PM6 and acceptor (BO-4Cl) to enhance the built-in electric field of the device and promote charge transport, thereby reducing charge recombination. As a result, the target device achieved an improved PCE of 18.03% compared to 17.24% for the control and demonstrated superior ambient stability, retaining 91% of its initial PCE after 1600 h in long-term shelf stability tests, whereas the control device retained 87%. These results confirm the effectiveness of PVDF-TrFE as an IEA that increases durability [21]. Chen et al. introduced a fatty acid solid additive with high solubility in chloroform into a PM6 donor layer to enable spontaneous diffusion during the subsequent acceptor deposition, which was processed using chloroform. This approach facilitated the refined pre-phase separation at the D-A interface. Consequently, the device exhibited a higher PCE than the control device (19.02% and 18.73%, respectively). This strategy, in which additives enable effective interfacial engineering, demonstrates the potential to overcome the limitations of traditional bulk heterojunction and layer-by-layer methods [1]. Although these studies confirmed the benefits of IEAs in OSCs, thereby limiting their broader applicability.

In this study, starburst-shaped TPA-based materials DTDCPB and DPDCPB were solution-processed onto pure PEDOT:PSS to fabricate highly efficient OSCs. DTDCPB and DPDCPB are suitable as hole transporters when used as donors [22]. When inserted between PEDOT:PSS and the active layer, they function as hole transporting auxiliaries (HTAs), offering the potential for dynamic interfacial engineering. The thin film of HTAs on PEDOT:PSS modulates the interfacial potential barrier, promoting exciton migration and allowing precise control over interfacial properties. The pre-deposited HTAs exhibited high solubility in the cast active layer solution, gradually dissolving and diffusing into the solution. This process not only suppressed the charge recombination within the active layer but also increased conductivity and charge transport. The PEDOT:PSS/DTDCPB and PEDOT:PSS/DPDCPB achieved PCEs of 17.54% and 17.24%, respectively, in Device 1 (D18/L8-BO), which were higher than the PCEs of 16.92% of the PEDOT:PSS based control device. The use of small-molecule HTAs increased the J_{SC} values.

More importantly, the best-performing DTDCPB-based OSCs (Device 1) demonstrated superior stability, as evidenced by systematic investigations of storage, thermal, and photostability, when compared to the control device. These results showed that DTDCPB enhanced crystallinity and balanced charge transport, resulting in more efficient charge mobility and stable device performance compared with the control device.

The low-bandgap DTDCPB and DPDCPB based on the D-A-A architecture exhibited strong absorption in the visible region. They effectively diffused into the subsequently cast active layer without compromising optical transmittance when used as HTAs, confirming their potential for interfacial engineering. Semitransparent organic solar cells (ST-OSCs) were previously fabricated using metal–oxide (MO) electrode structures composed of Ag and WO_3 [23]. Notably, the devices based on DTDCPB were optimized for PCE and average visible transmittance (AVT) using different active layer systems. The PEDOT:PSS/DTDCPB-based ST-OSCs achieved the highest light use efficiencies (LUEs), reaching 2.91%, 3.94%, and 3.12% for Devices 1, 2 (P(3IN = 0.3)(3IN2F = 0.5)(BDD = 0.2):BTP-eC9), and 3 (PTB7-Th:IEICO-4F), respectively compared with 2.84%, 3.72%, and 3.10% for the corresponding control devices. These results confirm that the incorporation of small-molecule-based HTAs facilitates effective diffusion into the active layer, thereby enabling the engineering of interfaces between the active layers and hole transport layers. Furthermore, these findings suggest that further exploration of diverse HTA materials could contribute to the development of both high-performance OSCs and high-quality ST-OSCs in the near future.

2. Experiments

2.1. Materials and synthesis

ITO glass (sheet resistance 10 Ω/square) were purchased from AMG (Republic of Korea). Poly(3,4-ethylenedioxythiophene):poly(styrenesulfonate) (PEDOT:PSS) (Clevious P VP AI 4083) and PEDOT:PSS (HTL Solar) were obtained from Heraeus (Germany) and used as

HTLs. DTDCPB and DPDCPB were synthesized according to literature procedures [22]. The donor and acceptor materials including D18, L8-BO, BTP-eC9, IEICO-4F, and PDINN were purchased from Derthon (China). PTB7-Th, used for transparent device fabrication, was acquired from 1-Material (Canada). P(3IN = 0.3)(3IN2F = 0.5)(BDD = 0.2) was synthesized according to the methods reported before [23]. Solvents including chlorobenzene (CB, 99.8%), chloroform (CF, $\geq$99%), *o*-xylene (XY, 97%), methanol (MeOH, $\geq$99.8%), and diiodomethane (DIM, 99%) were purchased from Sigma-Aldrich (USA). The solvent additive 1-chloronaphthalene (CN, 85%) was purchased from TCI (Japan). 1-phenylnaphthalene (PN; 97%) was from Alfa Aesar (USA).

2.1.1. Synthesis of 2-{[7-(4-N,N-ditolylaminophenylen-1-yl)-2,1,3-benzothiadiazol-4-yl]methylene}malononitrile (DTDCPB)

A mixture of 4-bromo-7-dicyanovinyl-2,1,3-benzothiadiazole (100 mg, 0.343 mmol), 4-(*N*,*N*-ditolylamino)-1-(tri-n-butylstannyl)phenylene (232 mg, 0.412 mmol), and $PdCl_2(PPh_3)_2$ (12 mg, 0.0171 mmol) was dissolved in 3 mL of anhydrous toluene. The reaction mixture was stirred under argon at 110 °C for 8 h. Upon completion, the reaction was cooled to room temperature, and the solvent was removed under reduced pressure. The crude product was purified by silica gel column chromatography using a mixture (dichloromethane:hexane = 4:3) as the eluent to afford DTDCPB as a black solid (80 mg, 51% yield). ^1H NMR ($CDCl_3$, 500 MHz) 8.82 (s, 1H), 8.78 (d, 1H), 7.95 (d, 2H), 7.84 (d, 1H), 7.14–7.08 (m, 10H), 2.34 (s, 6H)

2.1.2. Synthesis of 2-{[7-(4-N,N-diphenylaminophenylen-1-yl)-2,1,3-benzothiadiazol-4-yl]methylene}malononitrile (DPDCPB)

A mixture of 4-bromo-7-dicyanovinyl-2,1,3-benzothiadiazole (100 mg, 0.343 mmol), *N*,*N*-diphenyl-4-(tributylstannyl)aniline (220 mg, 0.412 mmol), and $PdCl_2(PPh_3)_2$ (12 mg, 0.0171 mmol) was dissolved in 3 mL of anhydrous toluene. The reaction was stirred under argon at 110 °C for 8 h. After completion, the mixture was cooled to room temperature and concentrated under reduced pressure to remove the solvent. The crude product was purified by silica gel column chromatography using a mixture (dichloromethane:hexane = 4:3) as the eluent to afford DPDCPB as a black solid (70 mg, 42% yield). ^1H NMR ($CDCl_3$, 500 MHz) 8.84 (s, 1H), 8.79 (d, 1H), 7.98 (d, 2H), 7.86 (d, 1H), 7.33 (m, 4H), 7.19 (m, 6H), 7.13 (t, 2H)

2.2. Solution preparation and device fabrication

2.2.1. Solution preparation

DTDCPB and DPDCPB solutions: DTDCPB and DPDCPB were dissolved in CF at a concentration of 3 mg mL^{-1}. The solutions were thermally treated on a 50 °C hotplate for 30 min prior to use.

Device 1 [D18/L8-BO]: D18 was dissolved in CB at a concentration of 6 mg mL^{-1}. L8-BO was dissolved in chloroform containing 0.25 vol% (v/v) DIM at a concentration of 8 mg mL^{-1}. The D18 solution was preheated at 100 °C before processing.

Device 2 [P(3IN = 0.3)(3IN2F = 0.5)(BDD = 0.2):BTP-eC9]: A blend with weight ratio (wt. ratio) of 1:1.2 was dissolved in XY containing 0.75 vol% PN at a total concentration of 27.6 mg mL^{-1}. The solution was preheated at 100 °C before deposition.

Device 3 [PTB7-Th:IEICO-4F]: PTB7-Th and IEICO-4F were blended in a 1:1 wt ratio at a concentration of 24 mg mL^{-1} in CB containing 0.5 vol% CN. This solution was preheated to 80 °C prior to film formation.

Electron Transport Layer (ETL) Solution: A total of 1 mg of PDINN was dissolved in 1 mL of MeOH at room temperature using a roll mixer for over 1 h inside a nitrogen glove box. The resulting solution was filtered through a 0.45 μm PTFE filter (25HP045AN).

2.2.2. Device fabrication

Control device: Conventional solar cells were fabricated with the configuration of ITO/PEDOT:PSS/active layer/PDINN/Ag structure. The patterned ITO glass was sequentially cleaned via ultrasonication in a detergent solution (Alconox Inc.), isopropanol, and deionized water for 10 min. The substrate was dried with a nitrogen gun, followed by thermal treatment at 100 °C for 10 min to ensure the complete removal of any remaining moisture. The cells were treated with a UV-ozone (UVO) cleaner (Ahtech LTS AH1700) for 20 min. The patterned ITO glass was spin-coated with diluted PEDOT:PSS (PEDOT:PSS:D. I. = 1:0.2), which was previously filtered through a 0.45 μm PTFE filter (25HP045AN) at 4500 rpm for 30 s under ambient conditions. The films were thermally annealed at 110 °C for 10 min. The active layers were spin-coated inside a nitrogen-filled glove box under the following conditions: D18/L8-BO (Device 1) was spin-coated at 1500–2000 rpm for D18 and at 4000 rpm for L8-BO, P(3IN = 0.3)(3IN2F = 0.5)(BDD = 0.2): BTP-eC9 (Device 2) at 4000–5000 rpm, and PTB7-Th:IEICO-4F (Device 3) at 1500–2000 rpm. All the coated substrates were thermally annealed at 100 °C for 10 min. The active layer formed, and PDINN was cast at 2000 rpm and dried at room temperature. Finally, the samples were transferred to a vacuum thermal evaporation system, where 100 nm of Ag was deposited at a rate of 1.0 Å/s (shadow mask area: 4.0 mm^2).

Small-molecule HTA based devices: The devices with the ITO/PEDOT:PSS/DTDCPB or DPDCPB/active layer/PDINN/Ag structure were fabricated using the same procedure as that for the control device. The prepared DTDCPB or DPDCPB solutions were spin-coated onto the PEDOT:PSS layer at 4000 rpm for 30 s.

ST-OSCs: e process for fabricating the ST-OSCs was identical to that of the opaque devices, except for the top electrode. The cathode was prepared through thermally evaporating 14 nm Ag at a rate of 2.0 Å/s, followed by depositing 30 nm WO_3 at a rate of 1.0 Å/s.

2.3. Characterization

The ^1H NMR spectra were collected using a JEOL 500 MHz/JNM-ECZ500 R/S spectrometer, with $CDCl_3$ as the solvent. Current density–voltage (*J*–*V*) characteristics were measured using a Keithley 2401 source meter. Simulated solar illumination at 100 mW cm^{-2} (AM 1.5G) was provided by a n ABA-rate solar simulator (Newport), calibrated with a 91150V Si reference cell (ORIEL). External quantum efficiency (EQE) spectra were recorded in ambient atmosphere using a Polaronix K3100 IPCE system (McScience, Republic of Korea). Photoluminescence (PL) spectra were analyzed using a PerkinElmer LS-55 spectrofluorometer. Absorption spectra and UV–Vis transmission were measured using a QEX7 system (in transmission mode) and an Agilent 8453 UV–Vis spectrophotometer, respectively. Based on these measurements, the AVT was calculated using Equation (1):

$$AVT = \frac{\int T(\lambda)F(\lambda)E(\lambda)d\lambda}{\int F(\lambda)E(\lambda)d\lambda} \tag{1}$$

where T is the transmittance spectrum, F is the photon flux of the standard solar spectrum, and E is the photopic response of the human eye in the 380–780 nm wavelength range [24]. The work functions of the thin films were measured using ultraviolet photoelectron spectroscopy (UPS) with a He I (21.2 eV) light source on an AXIS Ultra DLD system, conducted at the Korea Basic Science Institute (KBSI) in Daejeon. Crystalline orientation and molecular packing were examined by Two-dimensional grazing incidence wide-angle X-ray scattering (2D-GIWAXS), performed at the 3C beamline of the Pohang Accelerator Laboratory (PAL) to obtain high-quality images. Besides, surface topography and potential mapping were carried out using atomic force microscopy (AFM) and scanning Kelvin probe microscopy (SKPM), respectively. Both measurements were conducted in non-contact mode using a PSIA XE-100 instrument (Park Systems) with a scan area of 5 μm × 5 μm. The thicknesses of the active layers were measured using an Alpha step (TENCOR Alpha Step 500). For Device 1 (D18/L8-BO), the thickness of the PEDOT:PSS/Device 1 film ranged from 100 to 120 nm, while the PEDOT:PSS/DTDCPB/Device 1 film exhibited a thickness of

100 to 110 nm. For Device 2 (P(3IN = 0.3)(3IN2F = 0.5)(BDD = 0.2): BTP-eC9), the PEDOT:PSS/Device 2 film had a thickness of 60 to 80 nm, and the PEDOT:PSS/DTDCPB/Device 2 film ranged from 50 to 70 nm. For Device 3 (PTB7-Th:IEICO-4F), the thicknesses of the PEDOT: PSS/Device 3 and PEDOT:PSS/DTDCPB/Device 3 films were comparable, both measuring 50 to 70 nm. The time-of-flight secondary ion mass spectrometry (TOF-SIMS) analysis was performed using a TOF-SIMS 5 instrument (ION TOF). The thicknesses of TOF-SIMS were obtained using a surface profiler (P-6, KLA Tencor). Based on contact angle measurements conducted using a DSA100 contact angle analyzer (KRUSS) with deionized water and diiodomethane (DIM, 3.8 μL drop volume), the surface energy of the films was calculated according to Wu model. To measure the charge carrier mobilities of small-molecule HTAs, the space-charge-limited current (SCLC) method was used. For this purpose, hole-only and electron-only devices were fabricated with the architectures of ITO/PEDOT:PSS (AI 4083)/DTDCPB or DPDCPB/active layer/PEDOT:PSS (HTL Solar)/Ag and ITO/ZnO sol–gel/DTDCPB or DPDCPB/active layer/PDINN/Ag, respectively. The SCLC model was used to extract mobility values according to Equation (2).

$$J = \frac{9}{8}\varepsilon_0\varepsilon_r\mu\left(V^2 / d^3\right) \tag{2}$$

where μ is the charge carrier mobility, ε_r is the relative dielectric constant, ε_0 is the vacuum permittivity, V is the applied voltage, and d is the thickness.

3. Result & discussion

3.1. Characteristics and optical properties

Starburst-shaped D-A-A-type small-molecules containing TPA were synthesized according to a previously reported method [15]. The chemical structures of the two synthesized molecules, DTDCPB and DPDCPB, are shown in Fig. 1a, which were applied as small-molecule HTAs above the PEDOT:PSS film. DTDCPB and DPDCPB were previously used as donors in fullerene-based OSCs [16,22]; we thus hypothesized DTDCPB and DPDCPB would promote hole mobility when employed as HTAs. Scheme S1 shows that DTDCPB and DPDCPB were synthesized via Stille coupling reactions and subsequently characterized using ^{1}H NMR spectroscopy (Figs. S1 and S2), confirming the successful formation of the target compounds with yields of 51% for DTDCPB and 42% for DPDCPB. The thermal properties of these molecules, including the thermogravimetric analysis and differential scanning calorimetry results, were not analyzed in this study as these properties were previously reported [22].

Solubility tests were conducted for DTDCPB and DPDCPB, with the results summarized in Table S1. The tests were performed with a range of polar solvents, including methanol, isopropanol, and hexanol, as well as low-polarity solvents such as XY, CF, and CB. Both DTDCPB and DPDCPB exhibited limited solubility in most solvents at room temperature; however, they demonstrated significantly improved solubility in CF. The solubility of DTDCPB and DPDCPB increased in the following order at 50 °C: CB < XY < hexanol < CF. Consequently, CF was selected as the processing solvent for small-molecule HTAs due to its superior solubility at room temperature, which facilitated the formation of the most uniform films during the spin-coating process.

To investigate the optical properties of the two small-molecule HTAs, UV–Vis spectroscopy was performed. The normalized UV–Vis absorption spectra of the pristine DTDCPB and DPDCPB thin films are presented in Fig. 1b. The $\lambda_{\max}$ values of DTDCPB and DPDCPB were observed at 605 and 585 nm, respectively, indicating a 20 nm red-shifted for DTDCPB relative to DPDCPB. The optical bandgaps of DTDCPB and DPDCPB were estimated to be 2.05 and 2.12 eV, respectively. The bandgap of DTDCPB is narrower due to the presence of two methyl groups in its molecular structure. This finding is consistent with those of previous studies [22]. PL spectroscopy was conducted to indirectly assess the charge extraction characteristics following the introduction of each small-molecule HTA onto the PEDOT:PSS film (Fig. 1c). Three film configurations were prepared for comparison: ITO/PEDOT: PSS, ITO/PEDOT:PSS/DTDCPB, and ITO/PEDOT:PSS/DPDCPB. The emission intensity increased by approximately 1.2 times with DPDCPB

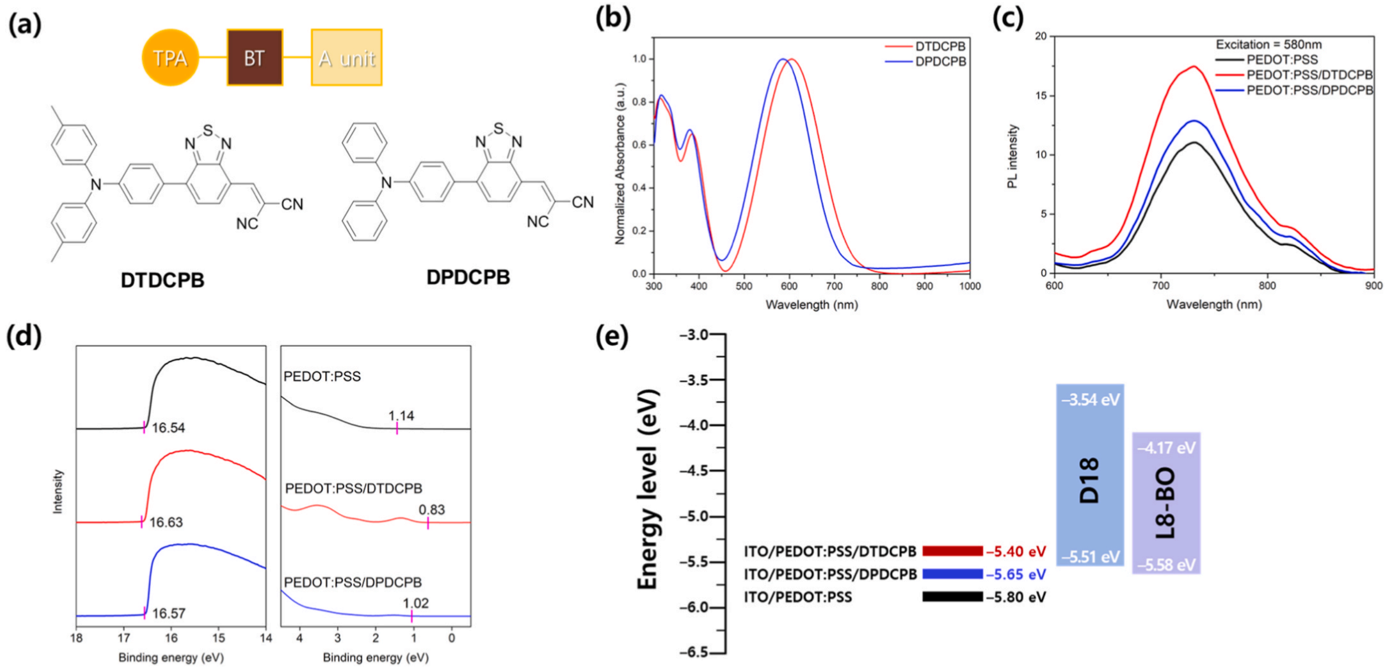

Fig. 1. (a) Chemical structures of DTDCPB and DPDCPB used, as small-molecule HTAs with PEDOT:PSS. (b) UV–Vis absorption spectra of ITO/PEDOT:PSS/DTDCPB and ITO/PEDOT:PSS/DPDCPB films. (c) PL spectra of PEDOT:PSS, PEDOT:PSS/DTDCPB, and PEDOT:PSS/DPDCPB films. (d) UPS characteristics of cut-off and on-set regions of PEDOT:PSS, PEDOT:PSS/DTDCPB, and PEDOT:PSS/DPDCPB films deposited on ITO substrate. (e) Energy-level diagram of PEDOT:PSS, PEDOT:PSS/DTDCPB, and PEDOT:PSS/DPDCPB films with active layer (D18 and L8-BO).

and 1.7 times with DTDCPB relative to the PEDOT:PSS film when excited at 580 nm. These results suggested that the small-molecule HTAs increased photon extraction [17].

UPS was used to investigate the effect of the small-molecule HTAs on the WF, and the results are shown in Fig. 1d. Thin films with the ITO/PEDOT:PSS, ITO/PEDOT:PSS/DTDCPB, and ITO/PEDOT:PSS/DPDCPB structures were prepared; the binding energies at the secondary electron cutoff region ($E_{cut-off}$) were 16.54, 16.63, and 16.57 eV, respectively; the Fermi edge values (E_{Femi}) were 1.14, 0.83, and 1.02 eV, respectively. The He(I) photon energy used for the UPS measurements was 21.22 eV. The absolute WF values were calculated using the following equation [25]:

$$|WF| = h\upsilon - \left(E_{cut-off} - E_{Femi}\right) \tag{3}$$

where $h\upsilon$ is the photon energy (21.22 eV), $E_{cut-off}$ is the cutoff energy, and E_{Femi} is the onset of the Fermi edge. The WF values were calculated as 5.80, 5.40, and 5.65 eV for the control, PEDOT:PSS/DTDCPB, and PEDOT:PSS/DPDCPB films, respectively. These results suggested that incorporating DTDCPB and DPDCPB into PEDOT:PSS increased the energy level alignment with the active layer (Device 1). The ability to modulate the WF contributed to increasing charge extraction and reducing charge recombination through lowering the interfacial energy barrier, leading to a slight increase in the V_{OC} slightly [26,27].

The surface electrical properties were investigated using a scanning Kelvin probe microscope (SKPM) technique. Based on the initial calibration using highly oriented pyrolytic graphite (HOPG), the work function (WF) of the samples was calculated based on the measured potential, as described in Equation (4) [27,28]:

$$\begin{aligned} &SKPM\ Work\ Function\ [eV] = 4.65 + surface\ potential\ (HOPG) \\ &\quad - surface\ potential(sample) \end{aligned} \tag{4}$$

As shown in Fig. S3, the SKPM-calculated WF for the control, PEDOT:PSS/DTDCPB, and PEDOT:PSS/DPDCPB films were 5.83, 5.69, and 5.48 eV, respectively. The trend in the SKPM results closely matched that observed in the UPS measurements, indicating the reliability and consistency of the experimental data. These findings, illustrated in the energy-level diagram in Fig. 1e, suggest that HTLs incorporating small-molecule HTAs can form energetically favorable interfaces for charge transport and extraction from the active materials such as D18 and L8-BO [18].

3.2. Photovoltaic performance of opaque OSCs with hybrid HTLs

The device architecture is illustrated in Fig. 2a, consisting of ITO/PEDOT:PSS/DTDCPB or DPDCPB/D18/L8-BO/PDINN/Ag. Specifically, D18 and L8-BO were deposited using the layer-by-layer (LBL) approach, designated as Device 1, which facilitates the formation of donor and acceptor interfaces. The devices utilizing hole transport agents (HTAs) of both DTDCPB and DPDCPB were optimized by varying their concentrations, as illustrated in Table S2. The optimized concentrations of DTDCPB and DPTDCPB solutions were confirmed at 3 mg mL^{-1}. The optimized thickness of both HTA materials was approximately 5 nm (Fig. S4). Importantly, the devices incorporating both HTAs exhibited remarkable thickness tolerance, suggesting that these materials might also be beneficial for the fabrication of large-area devices. The current density–voltage (*J*–*V*) characteristics of the optimized devices, which are shown in Fig. 2b. The corresponding photovoltaic parameters are listed in Table 1. Briefly, the control device exhibited a PCE of 16.92%

Table 1
Photovoltaic parameters of the optimized devices based on D18 and L8-BO (Device 1) with the control device and DTDCPB- or DPDCPB-based OSCs.

	J_{SC} [mA cm^{-2}]	J_{Cal}^{a} [mA cm^{-2}]	V_{OC} [V]	FF [%]	PCE$_{max}$/ PCE$_{ave}$^{b} [%]
PEDOT:PSS	24.74	23.98	0.877	78.00	16.92/16.92 ± 0.04
PEDOT:PSS/ DTDCPB	25.12	24.20	0.881	79.28	17.54/17.47 ± 0.05
PEDOT:PSS/ DPDCPB	25.07	24.08	0.879	78.26	17.24/17.18 ± 0.04

[a] J_{cal} values were obtained from EQE curves.;
[b] statistical data were obtained from 10 independent devices.

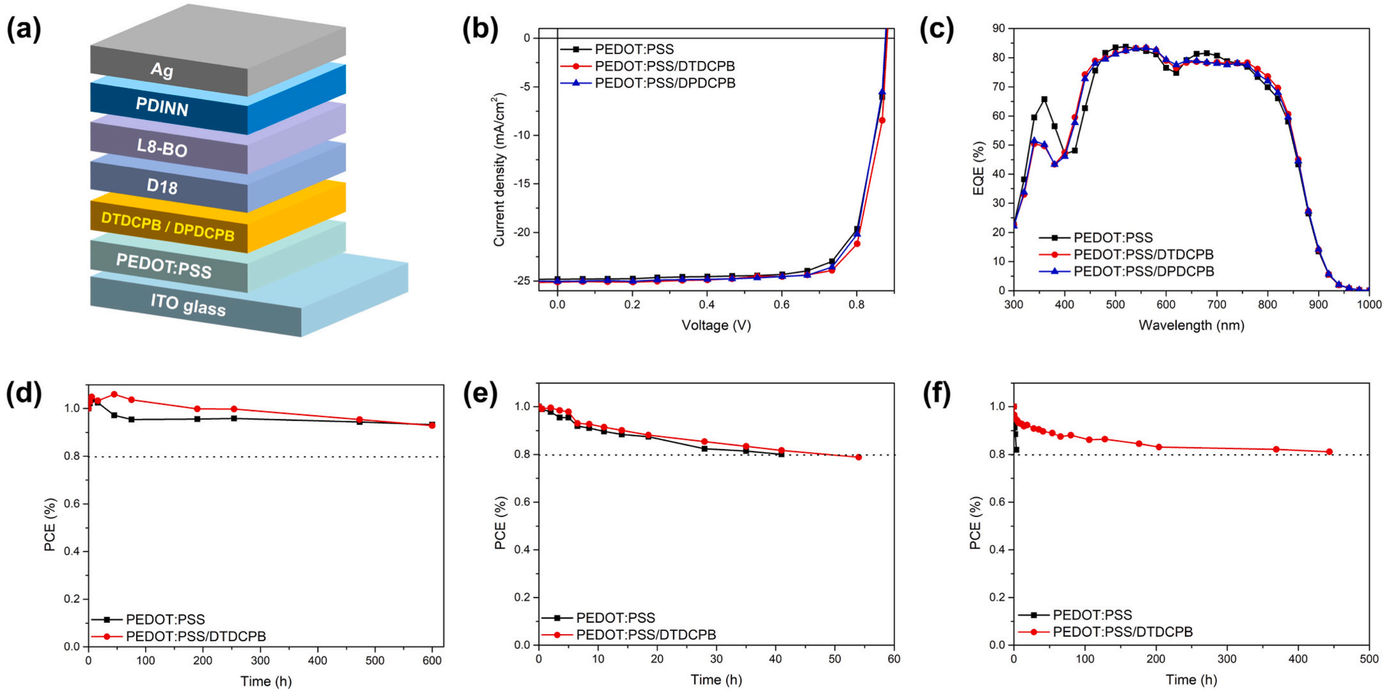

Fig. 2. (a) Device structure of OSCs featuring control device and HTAs OSCs (PEDOT:PSS/DTDCPB and PEDOT:PSS/DPDCPB). (b) Current density–voltage (*J*–*V*) and (c) EQE curves of the optimized devices based on D18 and L8-BO (Device 1) with control device and DTDCPB or DPDCPB based OSCs under AM 1.5G 1-sun (100 mW cm^{-2}) illumination. Stability test curves according to (d) ISOS-D1I, (e) ISOS-D2I, and (f) ISOS-L1 for optimized OSCs based on Device 1 with different HTLs.

($V_{OC} = 0.877$ V, $J_{SC} = 24.74$ mA cm^{-2}, FF = 78.00%). In contrast, the PEDOT:PSS/DTDCPB-based OSC achieved a PCE of 17.54% (V_{OC} = 0.881 V, J_{SC} = 25.12 mA cm^{-2}, FF = 79.28%), and the PEDOT:PSS/DPDCPB-based OSC had a PEC of 17.24% (V_{OC} = 0.879 V, J_{SC} = 25.07 mA cm^{-2}, FF = 78.26%). The PCE of the PEDOT:PSS/DTDCPB device was the highest, which was attributed to increased energy level alignment and hole transport, leading to simultaneous increases in J_{SC} and FF. The EQE measurement was used to verify the reliability of the *J*–*V*-derived J_{SC} values through integration and mismatch-factor analysis (Fig. 2c). The integrated J_{SC} values were 23.98, 24.20, and 24.08 mA cm^{-2} for the control, PEDOT:PSS/DTDCPB, and PEDOT:PSS/DPDCPB devices, respectively, all within 5% of the values obtained under standard AM 1.5G illumination. The devices with the small-molecule HTAs had higher EQE values in the 600–700 nm region than the control device, consistent with their optical absorption characteristics. This increase was likely due to the spectral overlap between the absorption of the small-molecule HTAs and that of the active layer [14]. Furthermore, an additional improvement in the range of 750–850 nm was observed, which might be attributed to the diffusion and penetration of the HTAs into the active layer during high-temperature annealing (~100 °C), which modulated the crystallinity of the donor phase and the overlying acceptor layer [21]. The increase in J_{SC} was also explained by the changes in the surface potential, the increased energy level alignment, and changes in the optical properties induced by incorporating small-molecule HTAs [4,5]. These findings indicated that the use of bilayer HTLs based on DTDCPB and DPDCPB enabled the regulation of the donor and/or acceptor interfaces even when the HTAs were partially dissolved or reconfigured during the solution deposition of the active layer. This interfacial regulation ultimately increased charge transport and extraction.

To further evaluate the stability of organic solar cell (OSC) devices incorporating various HTLs, encapsulated devices based on Device 1 were subjected to aging under different conditions: storage (ISOS-DI-1), thermal (ISOS-DI-2), and light-soaking (ISOS-L-1), in accordance with the protocols established by the International Summit on Hybrid and Organic Photovoltaic Stability (ISOS). As shown in Fig. 2d, the PEDOT:PSS/DTDCPB-based device presents an improved efficiency compared to its initial efficiency during the first 5 h. This is subsequently followed by a degradation trend akin to that observed in the PEDOT:PSS device. As illustrated in Fig. 2e, the thermal stability tests demonstrated that the

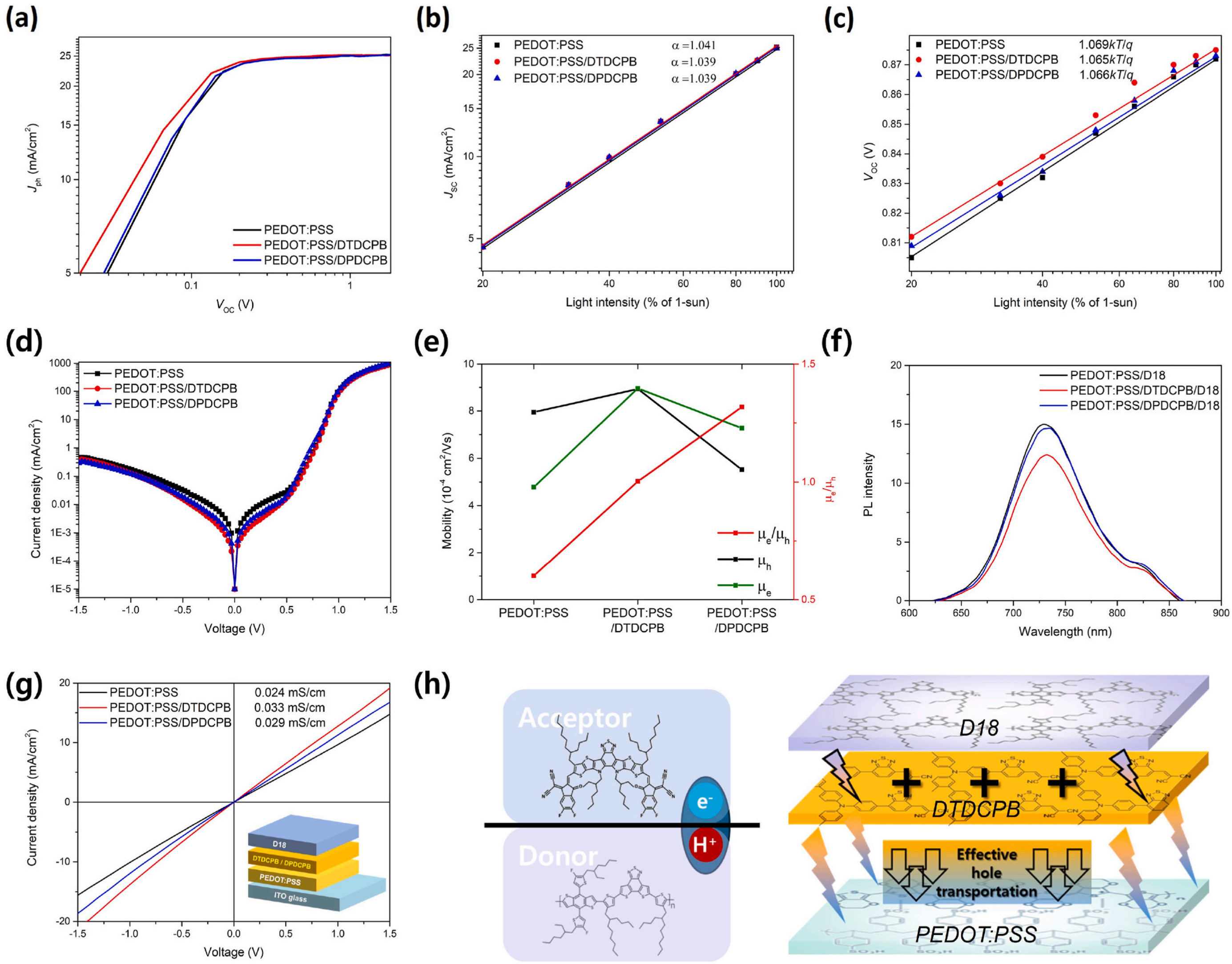

Fig. 3. (a) Photocurrent density–effective voltage (J_{ph}–V_{eff}), (b) J_{SC}–light intensity dependence, (c) V_{OC}–light intensity dependence, and (d) dark current density (J_D)–*V* characteristics of OSCs (Device 1) with the control device and DTDCPB or DPDCPB based OSCs. (e) Charge carrier mobility characteristics of hole- and electron-only control, DTDCPB-, or DPDCPB-based OSCs, measured using SCLC method. (f) PL spectra of ITO/PEDOT:PSS/D18, ITO/PEDOT:PSS/DTDCPB/D18, and ITO/PEDOT:PSS/DPDCPB/D18 films. (g) *I*–*V* curves of devices with ITO/PEDOT:PSS/DTDCPB or DPDCPB/D18/Ag structure. (h) Schematic diagram of active layer (D18 and L8-BO) and HTLs (DTDCPB and PEDOT:PSS).

PEDOT:PSS device achieved T_{80} (the time required to reach 80% of initial efficiency) after 41 h, while the PEDOT:PSS/DTDCPB device sustained its performance for up to 54 h, indicating slightly enhanced thermal durability. Surprisingly, as illustrated in Fig. 2f, under continuous illumination with a 1 sun LED source, the PEDOT:PSS/DTDCPB device reached T_{80} after 444 h, while the PEDOT:PSS device reached T_{80} after only 5 h, confirming the significantly enhanced photostability of the HTA-based device. This improvement can be attributed to the intrinsic photostability of the TPA core of DTDCPB, as reported in the literature [29–32]. These findings suggest that the strategically introduced HTA not only integrates effectively into the device architecture but also enhances environmental stability by diffusing into the active layer [31]. Consequently, HTA-based OSC devices exhibit advantages in both efficiency and stability under various environmental conditions.

3.3. Charge dynamics in small-molecule HTAs OSCs

The photocurrent density (J_{ph}) as a function of the effective applied voltage (V_{eff}) was measured for each device to further examine the impact of incorporating the small-molecule HTAs on the photovoltaic performance. J_{ph} is the difference between the current density under illumination J_L and in the dark J_D: $J_{\text{ph}} = J_L–J_D$. The effective voltage (V_{eff}) is calculated as $V_0–V_{\text{appl}}$, where V_0 is the voltage at which $J_{\text{ph}} = 0$, and V_{appl} is the applied bias. J_{ph} reached saturation at a V_{eff} of approximately 1.5 V (Fig. 3a). The maximum exciton generation rate (G_{max}) was estimated as follows:

$$J_{\text{sat}} = e \cdot L \cdot G_{\text{max}} \tag{5}$$

where J_{sat} is the saturation photocurrent density, e is the elementary charge, and L is the thickness of the active layer. The detailed G_{max} values and related data are summarized in Table S3. The control device had a G_{max} of 1.655×10^{28} m^{-3} s^{-1}. The G_{max} values of the PEDOT:PSS/DTDCPB- and PEDOT:PSS/DPDCPB-based OSCs were 1.657×10^{28} and 1.6578×10^{28} m^{-3} s^{-1}, respectively. These values indicated a marginally faster exciton generation rate of the HTA-incorporated devices, which correlated with the increased J_{SC} values. The exciton dissociation probability (P_{diss}) and charge collection probability (P_{coll}) were determined from the $J_{\text{ph}}/J_{\text{sat}}$ vs. V_{eff} and $J_{\text{mp}}/J_{\text{sat}}$ vs. V_{eff} curves, respectively, where J_{ph} and J_{mp} refer to the photocurrent densities under short-circuit and maximum power-point conditions, respectively. The P_{diss} values were 99.44%, 99.92%, and 99.45% for the control, PEDOT: PSS/DTDCPB, and PEDOT:PSS/DPDCPB devices, respectively. The PEDOT: PSS/DTDCPB-based OSCs exhibited the highest P_{diss}, which was ~0.5% higher than that of the control, indicating more efficient exciton dissociation. The P_{coll} value for the PEDOT:PSS/DTDCPB device was the highest, at 93.34%. These results highlighted the superior exciton dissociation and charge collection capabilities of the PEDOT: PSS/ DTDCPB-based OSCs, which contributed to the increase in J_{SC}.

The recombination kinetics of the control, PEDOT:PSS/DTDCPB-, and PEDOT:PSS/DPDCPB-based OSCs were investigated by measuring the $J–V$ characteristics under various light intensities (P_{light}), with the results shown in Fig. 3b and c. The relationship between J_{SC} and P_{light} follows a power law:

$$J_{\text{SC}} \propto P_{\text{light}}^{\alpha} \tag{6}$$

where α is an exponential factor derived from the slope of the $J_{\text{SC}}–P_{\text{light}}$ curve. An α value close to 1 indicates that bimolecular recombination is effectively suppressed within the device [11]. The PEDOT:PSS/DTDCPB and PEDOT:PSS/DPDCPB devices exhibited an α value of 1.039; the control device had a slightly higher value of 1.041 (Fig. 3b). This result suggested that introducing the small-molecule HTAs suppressed bimolecular recombination [33]. In particular, an α value approaching unity implies that the charge recombination within the device is low, indicating more-efficient exciton dissociation and charge extraction [12].

The trap-assisted recombination in the OSCs was evaluated by analyzing the relationship between V_{OC} and light intensity P_{light}, which is expressed as follows:

$$V_{\text{OC}} \propto n(kT/q)\ln(P_{\text{light}}) \tag{7}$$

where k, T, and q are the Boltzmann constant, absolute temperature, and elementary charge, respectively. A slope factor n approaching kT/q indicates negligible trap-assisted recombination, implying lower-density interfacial carrier traps and more efficient charge transport within the device [12,34]. The PEDOT:PSS/DTDCPB-and PEDOT: PSS/DPDCPB-based OSCs exhibited n values of 1.065 and 1.066, respectively, lower than that of the control device (1.069), as shown in Fig. 3c. This result indicates that the trap-assisted recombination for both small-molecule HTA-based devices was lower than that of the control, a finding that is consistent with previously reported exciton dissociation and charge collection characteristics [3].

The dark current density–voltage (J_D–V) characteristics were measured to investigate the origins of the differences in device performance (Fig. 3d). The PEDOT:PSS/DTDCPB- and PEDOT:PSS/DPDCPB-based OSCs exhibit similar reverse current behaviors to the control device in the voltage range of 0 to −1 V. The dark current of the PEDOT: PSS/DTDCPB device was the lowest in the forward bias region (0 to 0.5 V), indicating less leakage current and junction resistance [3,33,35]. Furthermore, the charge carrier mobilities were extracted using the space charge limited current mode to evaluate the effect of the small-molecule HTAs on the charge transport properties (Fig. 3e). The hole mobilities (μ_h) for the control, PEDOT:PSS/DTDCPB, and PEDOT: PSS/DPDCPB devices were calculated as 7.952×10^{-4}, 8.933×10^{-4}, and 5.522×10^{-4} cm^2 V^{-1} s^{-1}, respectively; the electron mobilities (μ_e) were 4.781×10^{-4}, 8.957×10^{-4}, and 7.272×10^{-4} cm^2 V^{-1} s^{-1}, respectively. The PEDOT:PSS/DTDCPB-based device had a μ_e/μ_h ratio of 1.003, indicating more balanced charge transport than the control (0.601) and PEDOT:PSS/DPDCPB (1.317) devices. This result suggests that the PEDOT: PSS/DTDCPB-based OSC possessed more balanced carrier transport properties, which is beneficial for increasing the J_{SC} and FF [4]. Additionally, PL spectroscopy was conducted to investigate whether introducing the small-molecule HTAs facilitated effective charge separation in the photoactive layer; the results are shown in Fig. 3f. The analysis focused on determining whether the charges generated in the polymer donor D18 were efficiently transferred to HTL. Excitation at the maximum absorption wavelength of the material could not be performed due to equipment limitations. However, the samples were excited at 580 nm, which is within the absorption range of D18. All samples exhibited a prominent emission peak at approximately 730 nm under this condition. The PL intensity of the control, PEDOT: PSS/DPDCPB- and PEDOT: PSS/DTDCPB-based devices were 15.03, 14.62, and 12.38, respectively, reductions of 2.7% and 17.6% compared with the control for DPDCPB and DTDCPB, respectively. These results suggested that the small-molecule HTAs promoted exciton dissociation through suppressing radiative recombination, with the most pronounced PL quenching observed in the DTDCPB-based device. Introducing the small-molecule HTAs into PEDOT:PSS increased photoinduced charge transfer and exciton dissociation within the D18 layer [5,17]. Furthermore, the finely tuned interfaces between the HTLs and donor layer enhanced the charge transport and extraction properties [4,20]. The electrical conductivity was measured to further study the effect of incorporating the small-molecule HTAs, with the results shown in Fig. 3g. The electrical conductivity was measured using the $I–V$ characteristics based on the ITO/PEDOT:PSS/D18/Ag (control) and ITO/PEDOT:PSS/HTAs/D18/Ag structures. The conductivity was calculated using the following equation:

$$I = \sigma A d^{-1} V \tag{8}$$

where A is the active area of the device, and d is the thickness of the film [12]. The conductivities of the control, PEDOT:PSS/DTDCPB, and PEDOT:PSS/DPDCPB devices were 0.024, 0.033, and 0.029 mS cm^{-1}, respectively. These findings indicate that incorporating the small-molecule HTAs facilitated hole transport toward the anode in the OSCs, enhancing device performance. As a result, the HTA-based OSCs improved intermolecular interactions between the photoactive layer and the hole transport layer via energetic cascade alignment and refined interface engineering. These features increased charge transport under reverse- and forward-bias conditions, ultimately increasing the J_{SC} and FF [36]. Fig. 3h shows that the small-molecule HTA layer partially penetrated and gradually diffused into the donor layer during the formation of the photoactive layer. This increased the charge separation at the donor, where the photogenerated carriers dissociated, and the resulting holes were transported along the donor domain. The HTAs allowed these holes to move through an optimized molecular pathway formed by the interpenetrated HTA layer [17,26]. This structural configuration increased charge transport and extraction owing to the increased hole mobility and overall conductivity of the device. Ultimately, this contributes positively to an improvement in the PCE.

3.4. Analysis of HTA surface morphology

We investigated the crystallinity, molecular orientation, and interfacial characteristics of the thin films to further study the causes of the enhanced electrical properties of the OSCs with the small-molecule HTAs. Two-dimensional grazing incidence wide-angle X-ray scattering (2D GIWAXS) and atomic force microscopy (AFM) were sequentially performed. First, GIWAXS was used to determine the relationship between the microcrystalline structures of the films and their charge transport properties under different conditions through measuring structural parameters. The full-width at half maximum (FWHM) values were extracted from the linear profiles of each GIWAXS image along the in-plane (IP) and out-of-plane (OOP) directions to calculate the crystalline coherence length (CCL) [37]. The CCL was calculated using the following equation:

$$CCL = 2\pi k / FWHM \tag{9}$$

where k is 0.9, and the FWHM represents the half-width of the diffraction peak. Detailed information on the parameters is summarized in Tables S4 and S5. Fig. 4a presents the 2D GIWAXS images of the PEDOT:PSS, PEDOT:PSS/DTDCPB, and PEDOT:PSS/DPDCPB films coated on Si substrates. All films exhibited a ring-like scattering pattern at q ≈ 1.23 Å^{-1}, corresponding to the randomly distributed PSS chains of PEDOT:PSS (Fig. S5c) [3,17,38,39]. The PEDOT:PSS (control film) and PEDOT:PSS/DPDCPB films showed no distinct scattering peaks; however, the PEDOT:PSS/DTDCPB film exhibited strong peaks at q ≈ 0.58 Å^{-1}, 0.84 Å^{-1}, 1.07 Å^{-1}, 1.65 Å^{-1}, and 1.77 Å^{-1} after accumulating the data in the in-plane and out-of-plane directions, indicating polycrystalline ordering characteristics (Fig. 4c and S5d).

The symmetric and enhanced crystallinity due to incorporating DTDCPB may facilitate the formation of a hierarchical or multi-length-scale morphology in the subsequently deposited active layer [40,41]. In addition, the incorporation of small-molecule HTAs into PEDOT:PSS resulted in a reduction of the (100) d-spacing observed in the OOP direction, decreasing from 22.56 to a range of 20.15–20.80 Å. Methylation has been shown to be an effective approach for enhancing crystallinity, as demonstrated in the literature [42–44]. The introduction of DTDCPB enhanced crystallinity by inducing broader diffraction peaks and more ordered molecular packing, thereby facilitating more compact lamellar stacking and improving vertical charge transport efficiency [21,22]. The surface morphologies of the films were analyzed using AFM. The root mean square (RMS) roughness values of PEDOT:PSS/DTDCPB and PEDOT:PSS/DPDCPB films were 0.687 and 0.741 nm, respectively (Fig. S6a–S6c), which were higher than that of the control film (0.594 nm). As illustrated in Fig. S5d–S5f, both films also exhibited more pronounced nanofibril-like surface morphology compared to the control film [36]. This morphology suggested that introducing small-molecule HTAs influenced the crystallinity, molecular orientation, and morphological properties of the subsequently formed active layers [45].

Subsequently, the 2D GIWAXS images and the corresponding linear profiles of the PEDOT:PSS/D18, PEDOT:PSS/DTDCPB/D18, and PEDOT:PSS/DPDCPB/D18 films were obtained (Fig. 4b and c). These measurements were used to determine the influence of the different HTLs on the crystallinity and molecular orientation characteristics of the polymer donor. Distinct crystalline peaks were observed for the PEDOT:PSS/D18 film along the IP direction at q ≈ 0.30, 0.52, and 1.03 Å^{-1}, corresponding to the (100), (002), and (004) planes, respectively. Additionally, a strong π–π stacking peak was observed at q ≈ 1.66 Å^{-1} along the OOP direction. These scattering features were attributed to the highly crystalline nature of D18, as previously reported [46]. A systematic decrease in the d-spacing values of the (100), (002), and (004) peaks was observed when D18 was deposited on small-molecule HTAs in the order of PEDOT:PSS/DPDCPB/D18 to PEDOT:PSS/DTDCPB/D18 compared with PEDOT:PSS/D18. This reduction in d-spacing suggested an increase in molecular packing, which increased hole transport [20,46]. Moreover, the results of analyzing the (010) peaks along the OOP direction for all films revealed that the DTDCPB-based film exhibited the

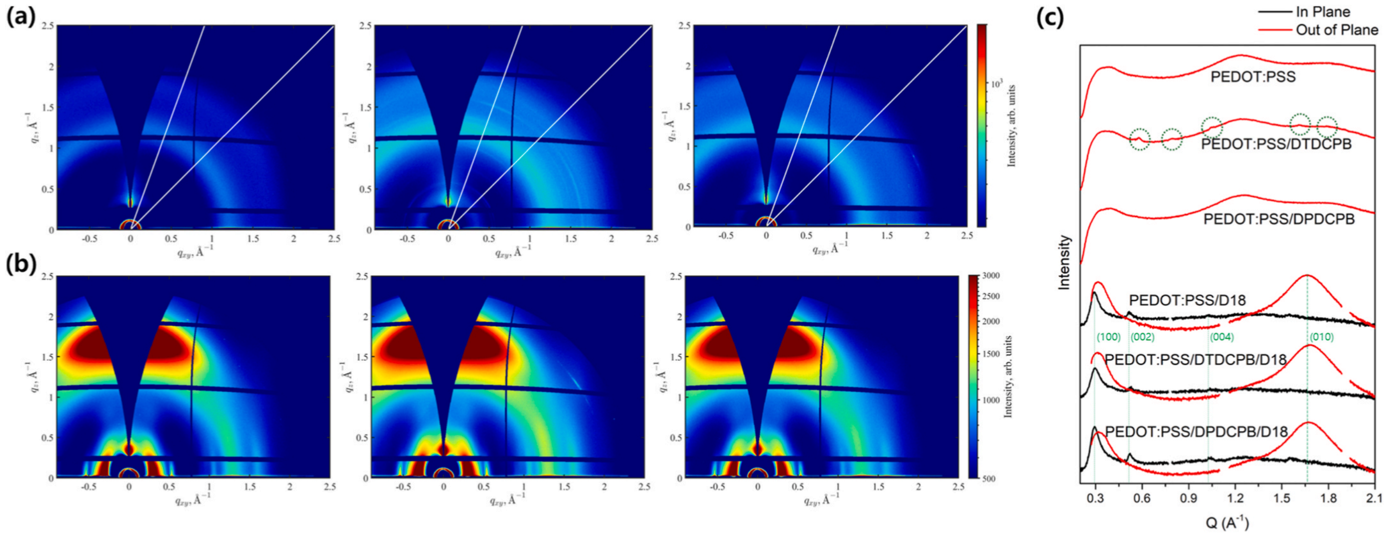

Fig. 4. (a) 2D GIWAXS patterns for different incident angles (20° and 45°) of control, DTDCPB, and DPDCPB films on a Si substrate. (b) 2D GIWAXS patterns of films with Si substrate/PEDOT:PSS/DTDCPB or DPDCPB/D18 configuration. (c) GIWAXS linecut profiles in out-of-plane and in-plane directions for (a) and (b).

narrowest π–π stacking distance of 3.74 Å and the largest CCL of 25.34 Å [11]. Furthermore, TPA-based small molecules effectively diffuse into the active layer, promoting enhanced π–π stacking and increased crystallinity [16,31]. Thus, introducing the small-molecule HTAs increased crystallinity through their diffusion and infiltration into the polymer film, thereby improving charge transport [34].

3.5. *Assessing the potential of HTA for ST-OSCs and universal testing*

Based on the results obtained from opaque devices, DTDCPB was demonstrated to be effective in Device 1. Given its promising potential, we proceeded to fabricate efficient ST-OSCs utilizing a range of donor–acceptor active layer systems. In the context of active layer systems, Device 1 utilized a D18/L8-BO combination, which was fabricated using the LBL technique. In contrast, Devices 2 and Device 3 employed bulk heterojunction (BHJ) structures, based on P(3IN = 0.3)(3IN2F = 0.5)(BDD = 0.2):BTP-eC9 and PTB7-Th:IEICO-4F blends, respectively. Device 2 and Device 3 were selected for their exceptional transparency in the visible region and their performance, which has been validated in the state-of-the-art ST-OSCs [23,47,48]. Table S6 and Table S7 were summarized as the optimized photovoltaic performance of the opaque devices incorporating PEDOT:PSS/DTDCPB for Devices 2 and 3. The J_{SC} of the PEDOT:PSS/DTDCPB devices was consistently higher than that of the control devices, which is similar to a trend observed in Device 1. Next, ST-OSCs for Devices 1, 2 and 3 were fabricated and comparatively analyzed. As simultaneously achieving PCE and high optical transmittance is essential for high-quality ST-OSCs [24], top electrode composition was carefully determined to get the best performance.

The MO structure was adopted as the top electrode to ensure high-transmittance ST-OSCs following previously reported procedures [23]. 14 nm Ag and 30 nm WO_3, were deposited via thermal evaporation in a sequence under vacuum conditions to form the transparent top electrode. ST-OSCs for Device 3 were fabricated with different HTLs under various preheating temperature conditions The ST-OSC structure was configured as ITO/PEDOT:PSS/DTDCPB/active layer/PDINN/Ag/WO_3, as illustrated in Fig. 5a. Detailed information on the active layer solutions and film fabrication was provided in experimental Section. The resulting ST-OSCs were optimized considering the PCE and AVT to maximize the LUE [23,24,49]. As a result, the *J–V* curves and photovoltaic characteristics (Fig. 5b and S7a) of the control and PEDOT:PSS/DTDCPB ST-OSCs were compared across the three active layer systems. The corresponding graphs comparing devices with and without the HTA for each system are presented in Fig. S7, while individual device results highlighting the presence or absence of HTA in each active layer system are additionally provided in Fig. S8. According to the photovoltaic parameters of the optimized ST-OSCs, the Device 1 ST-OSCs had a PCE of 12.11% (V_{OC} = 0.878 V, J_{SC} = 17.91 mA cm^{-2}), which was lower than that of the control (PCE = 12.42%, V_{OC} = 0.875 V, J_{SC} = 18.50 mA cm^{-2}. The Device 2 PCE was 9.15% (V_{OC} = 0.812 V, J_{SC} = 17.80 mA cm^{-2}), which was higher than that of the control (PCE = 9.06%, V_{OC} = 0.807 V, J_{SC} = 17.86 mA cm^{-2}). The PCE of Device 3 was 7.77% (V_{OC} = 0.716 V, J_{SC} = 17.52 mA cm^{-2}), which was also higher than that of the control (PCE = 7.38%, V_{OC} = 0.714 V, J_{SC} = 16.37 mA cm^{-2}).

Fig. 5c and S7b show the EQE and EQE + T + R spectra, respectively, where the integrated J_{cal} values from the EQE curves deviated within 5% of the measured J_{SC} values for the control and PEDOT:PSS/DTDCPB devices. The AVT was calculated over the visible wavelength range of 380 to 780 nm. The PEDOT:PSS/DTDCPB-based ST-OSCs for Devices 1, 2, and 3 exhibited AVTs of 24.00%, 43.10%, and 41.61%, respectively,

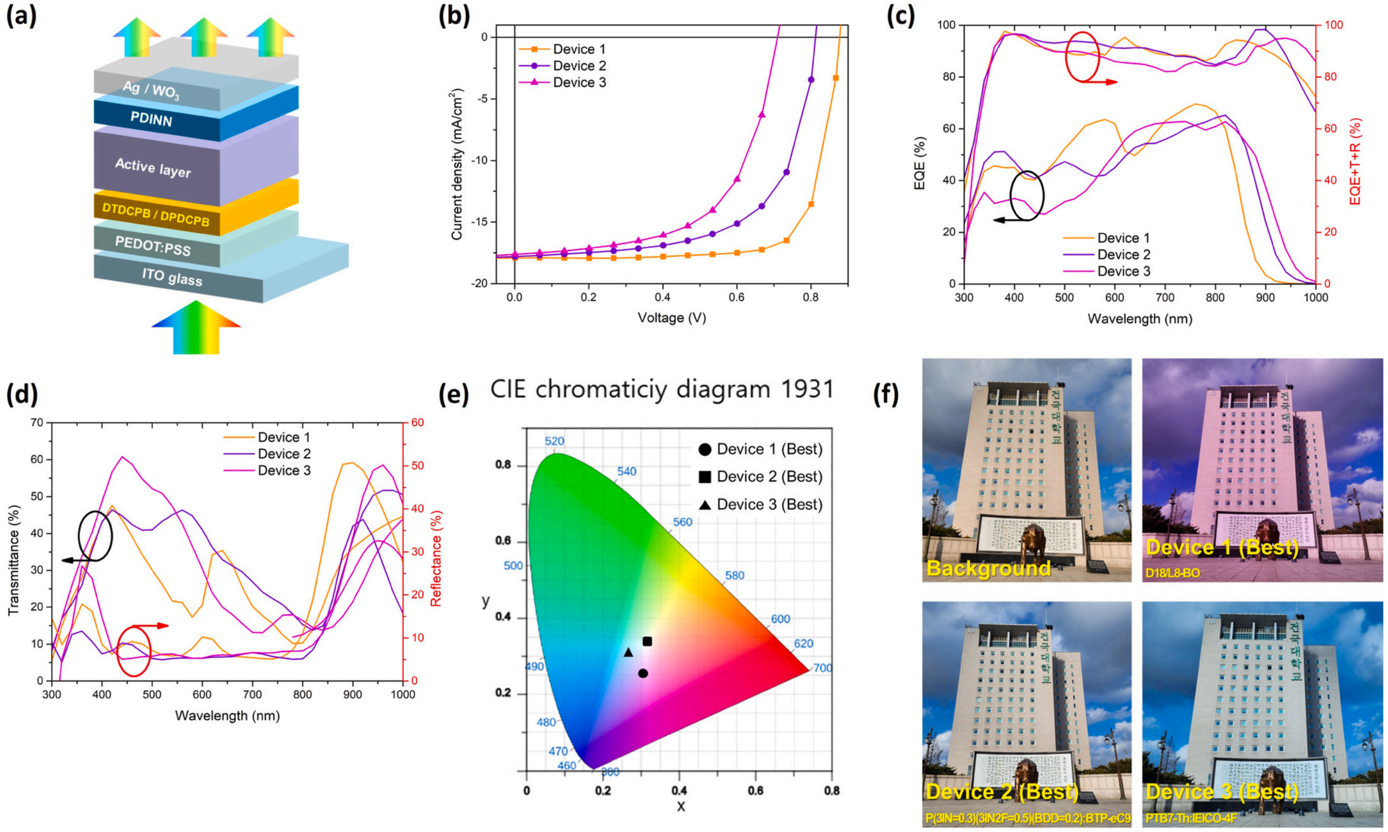

Fig. 5. (a) Device structure, (b) *J–V* characteristics, (c) EQE and EQE + T + R curves, and (d) transmittance and reflectance spectra of ST-OSCs with DTDCPB based OSCs based on active layers; Device 1 (D18/L8-BO), Device 2 (P(3IN = 0.3)(3IN2F = 0.5)(BDD = 0.2):BTP-eC9), and Device 3 (PTB7-Th:IEICO-4F). (e) Color coordinates of best-performing ST-OSCs with DTDCPB based OSCs on a CIE 1931 chromaticity diagram. (f) Photographs of corresponding ST-OSCs captured through device showing the background for Device 1, Device 2, and Device 3.

while the corresponding control devices showed AVTs of 22.90%, 41.11%, and 41.33% (Fig. 5d and S7c). These results indicate that the incorporation of the DTDCPB layer led to increased see-through function across all devices. Moreover, all the fabricated ST-OSCs had EQE + T + R values < 100%, confirming the reliability of the results [23]. The LUEs of the PEDOT:PSS/DTDCPB-based ST-OSCs for Devices 1, 2, and 3 were higher than those of the control devices in each active layer system, reaching 2.91%, 3.94%, and 3.12% respectively, compared with 2.84%, 3.72%, and 3.10% for the control devices. These results are summarized in Table 2 and confirm that DTDCPB effectively functioned as an HTA in each active layer system. This study provides guidelines for developing organic materials for efficient ST-OSCs and highlights their potential for practical applications [10].

The Commission Internationale d'Eclairage (CIE) 1931xyY chromaticity diagram was analyzed to evaluate the visual color perception of the PEDOT:PSS/DTDCPB ST-OSCs. Fig. 5e shows that the optimized PEDOT:PSS/DTDCPB ST-OSCs exhibited color coordinates (x, y) of (0.304 and 0.256) for Device 1, (0.316 and 0.337) for Device 2, and (0.270 and 0.306) for Device 3. Device 2 displayed color coordinates that were closest to the D65 white illuminant point (0.333, 0.333), suggesting considerable potential for window-integration applications. Notably, Devices 2 and 3 exhibited high color neutrality, indicating the synergistic effect of the PEDOT:PSS/DTDCPB-based ST-OSC strategy. Fig. 5f demonstrates the high color visibility of the PEDOT:PSS/DTDCPB ST-OSCs incorporating the three different active layer systems, through the devices. Consequently, introducing HTAs such as DTDCPB presents a new pathway for developing high-quality ST-OSCs, as supported by the LUE, the CIE 1931xyY chromaticity diagram, and visual transparency.

To further investigate the diffusion behavior of the HTA DTDCPB into the various active layers, TOF-SIMS depth profiling analysis was performed (Fig. S9). Nitrogen (N) signals were used to trace the diffusion of the HTA material. Among the three active layer systems studied, Device 1 was excluded from this analysis due to overlapping elemental signals between the donor material (D18) and the HTA (DTDCPB), which hindered reliable interpretation. Therefore, the active materials for Devices 2 and 3 without N atoms were selected for detailed evaluation. Fig. S9a–S9c show the results based on P(3IN = 0.3)(3IN2F = 0.5)(BDD = 0.2), the donor material of Device 2; Fig. S9d–S9f correspond to PTB7-Th, the donor of Device 3; and Fig. S9g–S9i present the results for the active layer blend of Device 2, P(3IN = 0.3)(3IN2F = 0.5)(BDD = 0.2):BTP-eC9. In Fig. S9c, the PEDOT:PSS/DTDCPB/P(3IN = 0.3)(3IN2F = 0.5)(BDD = 0.2) film exhibited a stronger N signal compared to the PEDOT:PSS/P(3IN = 0.3)(3IN2F = 0.5)(BDD = 0.2) film. As shown in Fig. S9f, the N signal intensity of the PEDOT:PSS/DTDCPB/PTB7-Th film was higher and more uniformly distributed across both the top and bottom interfaces compared to that of the PEDOT:PSS/PTB7-Th film. Notably, Fig. S9i illustrates that the N and CN signals are uniformly distributed throughout the active layer film of PEDOT:PSS/DTDCPB/P(3IN = 0.3)(3IN2F = 0.5)(BDD = 0.2):BTP-eC9, indicating effective interfacial diffusion when compared to the PEDOT:PSS/DTDCPB/P(3IN = 0.3)(3IN2F = 0.5)(BDD = 0.2) film. Collectively, these results demonstrate the diffusion behavior of DTDCPB into the active layer across each system from the PEDOT:PSS interface. This observation supports the potential for effective penetration of HTAs at the interface between the donor and acceptor materials [1,50].

To elucidate the reasons behind the enhanced AVT values observed in ST-OSCs incorporating DTDCPB compared to the control devices, we conducted a third-party analysis of the film thicknesses of the same samples used for TOF-SIMS, both with and without DTDCPB (Fig. S10). Neat donor materials for Device 2 and Device 3 were spin-coated onto ITO/PEDOT:PSS and ITO/PEDOT:PSS/DTDCPB substrates, respectively. As shown in Fig. S10, the thickness decreased in the HTA-based films from 32.8 nm to 26.2 nm for the donor of Device 2, from 54.5 nm to 38.7 nm for the donor of Device 3, and from 43.5 nm to 39.6 nm for the active layer of Device 2. The incorporation of HTA resulted in a significant reduction in film thickness in the organic layers of both Device 2 and Device 3 compared to their respective control devices, suggesting a diffusion derived from the DTDCPB into the donor layer decrease in thickness.

Furthermore, the active layer thicknesses for Devices 1–3 were rigorously re-evaluated using an Alpha Step surface profiler in our laboratory. For Device 1 (D18/L8-BO), the PEDOT:PSS/Device 1 film exhibited a thickness ranging from 100 to 120 nm, whereas the PEDOT:PSS/DTDCPB/Device 1 film ranged from 100 to 110 nm. In Device 2 (P(3IN = 0.3)(3IN2F = 0.5)(BDD = 0.2):BTP-eC9), the PEDOT:PSS/Device 2 film measured 60–80 nm, and the PEDOT:PSS/DTDCPB/Device 2 film was slightly thinner at 50–70 nm. For Device 3 (PTB7-Th:IEICO-4F), both the PEDOT:PSS and PEDOT:PSS/DTDCPB films showed comparable thicknesses in the range of 50–70 nm. The consistent reduction in film thickness measurements observed in HTA-based samples indicates that effective control of film processing conditions can promote HTA diffusion, resulting in thinner films and subsequently enhancing AVT of each active layer system, as illustrated in Fig. S11.

Contact angle (CA) measurements were conducted to investigate the wettability of ITO/PEDOT and ITO/PEDOT/DTDCPB films. As illustrated in Fig. S12, the contact angles of water and diiodomethane on the surface of the ITO/PEDOT/DTDCPB film were found to be 63.3° and 40.65°, respectively. This corresponds to a surface free energy of 56.1 mN/m, which represents a significant decrease compared to the ITO/PEDOT film (68.7 mN/m). The relevant parameters are summarized in Table S9. This finding suggests that the hydrophobicity of the PEDOT:PSS film is enhanced through the HTA strategy, which is advantageous for the wettability and interactions of the active layer. Given that organic semiconductors are typically dissolved in non-polar organic solvents, this increased hydrophobicity may improve compatibility with the hydrophobic organic active layer [51].

In this context, the HTA DTDCPB can be easily dissolved and rapidly mixed with the active material components (Device 1 and Device 2) when the active layer is deposited onto the ITO/PEDOT:PSS/DTDCPB film using processing solutions such as CB and XY that have been preheated to 100 °C. This suggests that the strong interactions between DTDCPB and the active materials facilitate the formation of high crystallinity and tight packing properties, as supported by the GIWAXS data obtained for the PEDOT:PSS/D18 and PEDOT:PSS/DTDCPB/D18 films

Table 2
Photovoltaic performances of the optimized ST-OSC devices based on Device 1, Device 2, and Device 3 with PEDOT:PSS and PEDOT:PSS/DTDCPB HTLs.

Active layer	HTL(or HTLs)	J_{SC} [mA cm^{-2}]	J_{Cal}[a)] [mA cm^{-2}]	V_{OC} [V]	FF [%]	PCE$_{\mathrm{max}}$/PCE$_{\mathrm{ave}}$[b)] [%]	AVT [%]	LUE[c)] [%]
Device 1	PEDOT:PSS	18.50	18.32	0.875	76.74	12.42/12.29 ± 0.09	22.90	2.84
	PEDOT:PSS/DTDCPB	17.91	17.75	0.878	77.02	12.11/11.95 ± 0.12	24.00	2.91
Device 2	PEDOT:PSS	17.86	17.85	0.807	62.85	9.06/9.01 ± 0.05	41.11	3.72
	PEDOT:PSS/DTDCPB	17.80	17.46	0.812	63.3	9.15/9.14 ± 0.03	43.10	3.94
Device 3[d)]	PEDOT:PSS	17.48	16.86	0.698	62.61	7.64/7.56 ± 0.05	41.33	3.10
	PEDOT:PSS/DTDCPB	17.62	17.23	0.710	60.02	7.50/7.41 ± 0.06	41.61	3.12

[a)] J_{cal} values were obtained from the EQE curves;
[b)] Statistical data were obtained from 5 independent devices;
[c)] Light utilization efficiency (LUE), LUE = PCE × AVT.
[d)] Statistical data were obtained from 10 independent devices.

mentioned above. However, for Device 3, the processing solvent CB was applied at a lower temperature of 80 °C, in contrast to the processing temperatures of 100 °C used for the CB and XY solutions in Device 1 and Device 2, respectively. Following the above-mentioned solubility test for DTDCPB at 50 °C, the solubility in CB is the worst. Overall, the results indicate that the HTA strategy was less effective in Device 3 compared to Devices 1 and 2. Nevertheless, we maintain that the HTA strategy can be effectively implemented by utilizing standardized optimized conditions—such as concentration, solvent/additive, and annealing temperature—for various active layer solutions. This approach has the potential to reduce the time required for device engineering optimization.

4. Conclusions

Starburst-shaped TPA-based small molecules DTDCPB and DPDCPB were introduced as HTAs on top of PEDOT:PSS to produce efficient ST-OSCs. The energy levels were more aligned in PEDOT:PSS/DTDCPB and PEDOT:PSS/DPDCPB films than in the control film, forming a cascade structure between the HTL and the active layer, which increased charge extraction. Furthermore, the results of conductivity analysis and charge transport characterization confirmed that introducing the small-molecule HTAs substantially enhanced charge transport. The PCE of the PEDOT:PSS/DTDCPB-based device was the highest among the OSCs (Device 1), achieving a value of 17.54%. Notably, the inherent structural features of the TPA core in DTDCPB contributed to enhanced photostability, achieving a T_{80} value of 444 h, which is significantly higher than that of the control device (5 h). The universality of the ST-OSCs was evaluated using different active layer systems to further validate the HTA effect of DTDCPB. The LUEs of the PEDOT:PSS/DTDCPB-based ST-OSC devices were higher than those of the control devices for each active layer system. For Device 1, the PCE and AVT of the ST-OSCs incorporating PEDOT:PSS/DTDCPB were 12.11% and 24.00%, respectively, leading to an LUE of 2.91%, which was an increased compared with control device (12.42% PCE, 22.90% AVT, 2.84% LUE). The PEDOT:PSS/DTDCPB-based ST-OSC for Device 2 had a PCE of 9.15% and an AVT of 43.10%, resulting in an LUE of 3.94%, outperforming the control device (9.06% PCE, 41.11% AVT, 3.72% LUE). Lastly, the PEDOT:PSS/DTDCPB-based ST-OSC for Device 3 had a PCE of 7.50% and an AVT of 41.61%, resulting in an LUE of 3.12%, outperforming the control device (7.64% PCE, 41.33% AVT, 3.10% LUE). Comprehensively, this study provides a promising and simple strategy for developing high-performance ST-OSCs for practical applications, primarily attributed to the effective diffusion behavior of the HTA. The approach is close to a universal method, and the incorporation of HTA represents a rational choice for enhancing long-term device stability.

CRediT authorship contribution statement

Ji Youn Kim: Writing – original draft, Formal analysis, Conceptualization, Investigation, Data curation. **Sung Jae Jeon:** Writing – review & editing, Formal analysis, Writing – original draft, Data curation. **Nam Gyu Yang:** Formal analysis, Data curation. **Ye Chan Kim:** Formal analysis, Data curation. **Doo Kyung Moon:** Writing – review & editing, Project administration, Supervision, Funding acquisition.

Declaration of competing interest

The authors declare that they have no known competing financial interests or personal relationships that could have appeared to influence the work reported in this paper.

Acknowledgements

This paper was supported in part by Human Resources Development Program of the Korea Institute of Energy Technology Evaluation and Planning (KETEP) grant funded by the Ministry of Trade, Industry and Energy, Republic of Korea (No. RS-2023-00237035). Also, this study is the result of a research project conducted with the funds of the Open R&D program of Korea Electric Power Corporation (R23XH02).

Appendix A. Supplementary data

Supplementary data to this article can be found online at https://doi.org/10.1016/j.mtener.2025.102029.

Data availability

No data was used for the research described in the article.

References

[1] G. Ding, T. Chen, M. Wang, X. Xia, C. He, X. Zheng, Y. Li, D. Zhou, X. Lu, L. Zuo, Z. Xu, H. Chen, Solid additive-assisted layer-by-layer processing for 19% efficiency binary organic solar cells, Nano-Micro Lett. 15 (2023) 92, https://doi.org/10.1007/s40820-023-01057-x.

[2] H. Li, Y. Li, X. Dai, X. Xu, Q. Peng, Ethanol processable inorganic-organic hybrid hole transporting layers enabled 20.12 % efficiency organic solar cells, Angew. Chem. Int. Ed. 64 (2025) 2300057, https://doi.org/10.1002/anie.202416866.

[3] X. Sun, J. Lv, X. Ding, C. Gao, G. Zhang, J. Zeng, C. Zou, W. Liu, S. Zhao, X. Ouyang, C. Yang, H. Hu, H. Chen, Enhancing efficiency and photo-stability of organic solar cells via vertical phase separation morphology induced by surface modification of PEDOT:PSS with star-shaped benzene-based DFTAB additive, ACS Mater. Lett. 6 (2024) 3282–3290, https://doi.org/10.1021/acsmaterialslett.4c00844.

[4] T. Huang, Y. Zhang, J. Wang, Z. Cao, S. Geng, H. Guan, D. Wang, Z. Zhang, Q. Liao, J. Zhang, Dual-donor organic solar cells with 19.13% efficiency through optimized active layer crystallization behavior, Nano Energy 121 (2024) 109226, https://doi.org/10.1016/j.nanoen.2023.109226.

[5] J. Wang, H. Yu, C. Hou, J. Zhang, Solution-processable PEDOT:PSS:α-In $_2$ Se $_3$ with enhanced conductivity as a hole transport layer for high-performance polymer solar cells, ACS Appl. Mater. Interfaces 12 (2020) 26543–26554, https://doi.org/10.1021/acsami.0c02489.

[6] C. Song, X. Huang, T. Zhan, L. Ding, Y. Li, X. Xue, X. Lin, H. Peng, P. Cai, C. Duan, J. Chen, Annealing-insensitive, alcohol-processed MoO $_x$ hole transport layer for universally enabling high-performance conventional and inverted organic solar cells, ACS Appl. Mater. Interfaces 14 (2022) 40851–40861, https://doi.org/10.1021/acsami.2c09413.

[7] M. Zeng, W. Zhu, J. Luo, N. Song, Y. Li, Z. Chen, Y. Zhang, Z. Wang, W. Liang, B. Guo, K. Zhang, F. Huang, Y. Cao, Highly efficient nonfullerene organic solar cells with a self-doped water-soluble neutral polyaniline as hole transport layer, Sol. RRL 5 (2021) 2000625, https://doi.org/10.1002/solr.202000625.

[8] L. Liu, L. Wu, H. Yang, H. Ge, J. Xie, K. Cao, G. Cheng, S. Chen, Conductivity and stability enhancement of PEDOT:PSS electrodes *via* facile doping of sodium 3-Methylsalicylate for highly efficient flexible organic light-emitting diodes, ACS Appl. Mater. Interfaces 14 (2022) 1615–1625, https://doi.org/10.1021/acsami.1c21591.

[9] J. Wan, R. Wen, Y. Xia, M. Dai, H. Huang, L. Xue, Z. Zhang, J. Fang, K.N. Hui, X. Fan, All annealing-free solution-processed highly flexible organic solar cells, J Mater Chem A Mater 9 (2021) 5425–5433, https://doi.org/10.1039/D0TA11831A.

[10] H. Chen, Z. Yin, Y. Ma, D. Cai, Q. Zheng, Solution-processed polymer bilayer heterostructures as hole-transport layers for high-performance opaque and semitransparent organic solar cells, Mater. Today Energy 35 (2023) 101322, https://doi.org/10.1016/j.mtener.2023.101322.

[11] J.H. Kim, Y.C. Kim, J.Y. Kim, H.S. Lee, Y.W. Han, H.W. Lee, D.K. Moon, In/Outdoor organic solar cells with effective photon-harvesting by introducing light-amplification layer with eco-friendly QDs, Small Struct. 4 (2023) 2300057, https://doi.org/10.1002/sstr.202300057.

[12] J. Zhang, L. Zhang, J. Chen, Polypyrrole-decorated hybrid anode interlayer for enhancing efficiency and stability of non-fullerene solar cells, ACS Appl. Polym. Mater. 6 (2024) 7742–7750, https://doi.org/10.1021/acsapm.4c01206.

[13] Y. Bao, H. Feng, X. Chen, Z. Liu, Z. Li, Y. Wang, B. Zhao, S. Liu, X. Zhang, W. Wu, C. Gao, Magnetic nanocomposite modified hybrid hole-transport layer for constructing organic solar cells with high efficiencies, ACS Appl. Mater. Interfaces 16 (2024) 54081–54091, https://doi.org/10.1021/acsami.4c15255.

[14] S. Chatterjee, N. Shimohara, T. Seo, S. Jinnai, T. Moriyama, M. Saida, K. Omote, K. Hama, Y. Iimuro, Y. Watanabe, Y. Ie, Green-light wavelength-selective organic solar cells: module fabrication and crop evaluation towards agrivoltaics, Mater. Today Energy 45 (2024) 101673, https://doi.org/10.1016/j.mtener.2024.101673.

[15] J. Wang, K. Liu, L. Ma, X. Zhan, Triarylamine: versatile platform for organic, dye-sensitized, and perovskite solar cells, Chem Rev 116 (2016) 14675–14725, https://doi.org/10.1021/acs.chemrev.6b00432.

[16] P. Agarwala, D. Kabra, A review on triphenylamine (TPA) based organic hole transport materials (HTMs) for dye sensitized solar cells (DSSCs) and perovskite solar cells (PSCs): evolution and molecular engineering, J Mater Chem A Mater 5 (2017) 1348–1373, https://doi.org/10.1039/C6TA08449D.

[17] B. Zhao, X. Huang, S. Chung, M. Zhang, Y. Zhong, A. Liang, Z. Zhao, C. Zhu, J. Zhao, S. Kim, J. Kim, M. Wang, S. Chen, K. Cho, Y. Wang, Z. Kan, Hole-selective-molecule doping improves the layer thickness tolerance of PEDOT:PSS for efficient organic solar cells, eScience 5 (2025) 100305, https://doi.org/10.1016/j.esci.2024.100305.

[18] S. Luo, C. Li, J. Zhang, X. Zou, H. Zhao, K. Ding, H. Huang, J. Song, J. Yi, H. Yu, K. S. Wong, G. Zhang, H. Ade, W. Ma, H. Hu, Y. Sun, H. Yan, Auxiliary sequential deposition enables 19%-efficiency organic solar cells processed from halogen-free solvents, Nat. Commun. 14 (2023) 6964, https://doi.org/10.1038/s41467-023-41978-0.

[19] Q. Chen, Z. Bian, Y. Yang, X. Cui, C. Jeffreys, X. Xu, W. Li, Y. Liu, M. Heeney, Z. Bo, Hierarchical solid-additive strategy for achieving layer-by-layer organic solar cells with over 19 % efficiency, Angew. Chem. Int. Ed. 63 (2024) e202405949, https://doi.org/10.1002/anie.202405949.

[20] Y. Wei, J. Yu, L. Qin, H. Chen, X. Wu, Z. Wei, X. Zhang, Z. Xiao, L. Ding, F. Gao, H. Huang, A universal method for constructing high efficiency organic solar cells with stacked structures, Energy Environ. Sci. 14 (2021) 2314–2321, https://doi.org/10.1039/D0EE03490H.

[21] J. Wang, Y. Li, F. Bi, C. Yang, M. Vasilopoulou, J. Chu, X. Bao, Revealing intrinsic free charge generation: promoting the construction of over 19% efficient planar p-n heterojunction organic solar cells, Angew. Chem. Int. Ed. 64 (2025) e202417143, https://doi.org/10.1002/anie.202417143.

[22] Y.-H. Chen, L.-Y. Lin, C.-W. Lu, F. Lin, Z.-Y. Huang, H.-W. Lin, P.-H. Wang, Y.-H. Liu, K.-T. Wong, J. Wen, D.J. Miller, S.B. Darling, Vacuum-deposited small-molecule organic solar cells with high power conversion efficiencies by judicious molecular design and device optimization, J. Am. Chem. Soc. 134 (2012) 13616–13623, https://doi.org/10.1021/ja301872s.

[23] S.J. Jeon, Y.C. Kim, J.Y. Kim, J.H. Kim, N.G. Yang, Y.J. Lee, H.S. Lee, Y.H. Kim, G. W. Kim, E.M. Jang, B. Lee, C. Yang, D.K. Moon, Molecular design of cost-effective donor polymers with high visible transmission for eco-friendly and efficient semitransparent organic solar cells, Chem. Eng. J. 472 (2023) 144850, https://doi.org/10.1016/j.cej.2023.144850.

[24] G.P. Kini, S.J. Jeon, D.K. Moon, Latest progress on photoabsorbent materials for multifunctional semitransparent organic solar cells, Adv. Funct. Mater. 31 (2021) 2007931, https://doi.org/10.1002/adfm.202007931.

[25] Y. Zhao, J. Chen, W. Chen, D. Ma, Poly(3,4-ethylenedioxythiophene):poly(styrenesulfonate)/MoO3 composite layer for efficient and stable hole injection in organic semiconductors, J. Appl. Phys. 111 (2012) 043716, https://doi.org/10.1063/1.3687933.

[26] W. Wang, Z. Lin, X. Li, C. Zhang, T. Yang, Y. Liang, Combining ZnO and PDINO as a thick cathode interface layer for polymer solar cells, ACS Appl. Mater. Interfaces 14 (2022) 18736–18743, https://doi.org/10.1021/acsami.2c01826.

[27] H. Li, J. Tan, S. Yang, Y. Sun, H. Yu, *P* -Toluenesulfonic acid modified two-dimensional $ZrSe_2$ as a hole transport layer for high-performance organic solar cells, ACS Appl. Mater. Interfaces 16 (2024) 20443–20453, https://doi.org/10.1021/acsami.4c00928.

[28] D.S. Mann, S. Thakur, S.S. Sangale, K.-U. Jeong, S.-N. Kwon, S.-I. Na, Antisolvent additive engineering containing green additive for efficient and stable perovskite solar cells, Sol. Energy Mater. Sol. Cell. 269 (2024) 112768, https://doi.org/10.1016/j.solmat.2024.112768.

[29] B. Liu, Z. Luo, S. Si, X. Zhou, C. Pan, L. Wang, A photostable triphenylamine-based flavonoid dye: solvatochromism, aggregation-induced emission enhancement, fabrication of organic nanodots, and cell imaging applications, Dyes Pigments 142 (2017) 32–38, https://doi.org/10.1016/j.dyepig.2017.03.023.

[30] J. Min, Y.N. Luponosov, C. Cui, B. Kan, H. Chen, X. Wan, Y. Chen, S. A. Ponomarenko, Y. Li, C.J. Brabec, Evaluation of electron donor materials for solution-processed organic solar cells via a novel figure of merit, Adv. Energy Mater. 7 (2017) 1700465, https://doi.org/10.1002/aenm.201700465.

[31] B. Chen, M. An, Y. Li, X. Wang, Z. Qiu, L. Dai, K. Cao, K. Yang, D. Yun, L. Deng, S. Xie, L. Zheng, Vacuum-deposited organic solar cells with over 10% efficiency and device lifetime over 2 years enabled by fluorinated donor, Adv. Funct. Mater. (2025) e09380, https://doi.org/10.1002/adfm.202509380.

[32] T. Lv, W. Zhang, Y. Yang, J. Zhang, M. Yin, Z. Yin, K. Yong, Q. An, Micro/Nano-Fabrication of flexible Poly(3,4-Ethylenedioxythiophene)-Based conductive films for high-performance microdevices, Small 19 (2023) 2301071, https://doi.org/10.1002/smll.202301071.

[33] Y. Lin, B. Adilbekova, Y. Firdaus, E. Yengel, H. Faber, M. Sajjad, X. Zheng, E. Yarali, A. Seitkhan, O.M. Bakr, A. El-Labban, U. Schwingenschlögl, V. Tung, I. McCulloch, F. Laquai, T.D. Anthopoulos, 17% efficient organic solar cells based on liquid exfoliated WS_2 as a replacement for PEDOT:PSS, Adv. Mater. 31 (2019) 1902965, https://doi.org/10.1002/adma.201902965.

[34] X. Yu, H. Lin, M. Li, B. Ma, R. Zhang, X. Du, C. Zheng, G. Yang, S. Tao, Ternary organic solar cells with enhanced charge transfer and stability combining the advantages of polymer acceptors and fullerene acceptors, Org. Electron. 104 (2022) 106471, https://doi.org/10.1016/j.orgel.2022.106471.

[35] W. Wang, W. Zhong, Z. Li, X. Li, Y. Tang, X. Yang, X. Wang, Y. Zhu, X. Zhang, Z. He, T. Yang, Y. Liang, A low-temperature solution-processed nickel oxide nanoparticles and phosphotungstic acid composite as an anode interface layer for organic solar cells, ACS Appl. Energy Mater. 7 (2024) 5120–5126, https://doi.org/10.1021/acsaem.4c00349.

[36] Y.W. Han, H.S. Lee, D.K. Moon, Printable and semitransparent nonfullerene organic solar modules over 30 cm^2 introducing an energy-level controllable hole transport layer, ACS Appl. Mater. Interfaces 13 (2021) 19085–19098, https://doi.org/10.1021/acsami.1c01021.

[37] G.P. Kini, S.J. Jeon, D.K. Moon, Design principles and synergistic effects of chlorination on a conjugated backbone for efficient organic photovoltaics: a critical review, Adv. Mater. 32 (2020) 1906175, https://doi.org/10.1002/adma.201906175.

[38] J. Dong, G. Portale, Role of the processing solvent on the electrical conductivity of PEDOT:PSS, Adv. Mater. Interfac. 7 (2020) 2000641, https://doi.org/10.1002/admi.202000641.

[39] T. Ki, C. Jang, J.S. Jin, J. Kim, N. Kim, H. Moon, S.-Y. Jang, S. Kwon, J. Jang, H. Kang, K. Lee, In situ doping of the PEDOT top electrode for all-solution-processed semitransparent organic solar cells, ACS Appl. Mater. Interfaces 15 (2023) 47317–47326, https://doi.org/10.1021/acsami.3c09984.

[40] J. Xu, S.B. Jo, X. Chen, G. Zhou, M. Zhang, X. Shi, F. Lin, L. Zhu, T. Hao, K. Gao, Y. Zou, X. Su, W. Feng, A.K.Y. Jen, Y. Zhang, F. Liu, The molecular ordering and double-channel carrier generation of nonfullerene photovoltaics within multi-length-scale morphology, Adv. Mater. 34 (2022) 2108317, https://doi.org/10.1002/adma.202108317.

[41] S.J. Jeon, N.G. Yang, Y.H. Kim, J.H. Yun, D.K. Moon, Bihalogenated thiophene-based terpolymers for high-performance semitransparent organic solar cells processed by an eco-friendly solvent and layer-by-layer deposition, ACS Appl. Mater. Interfaces 14 (2022) 38031–38047, https://doi.org/10.1021/acsami.2c10286.

[42] W. Wei, C. Zhang, Z. Chen, W. Chen, G. Ran, G. Pan, W. Zhang, P. Müller-Buschbaum, Z. Bo, C. Yang, Z. Luo, Precise methylation yields acceptor with hydrogen-bonding network for high-efficiency and thermally stable polymer solar cells, Angew. Chem. Int. Ed. 63 (2024) e202315625, https://doi.org/10.1002/anie.202315625.

[43] S. Li, L. Ye, W. Zhao, S. Zhang, S. Mukherjee, H. Ade, J. Hou, Energy-level modulation of small-molecule electron acceptors to achieve over 12% efficiency in polymer solar cells, Adv. Mater. 28 (2016) 9423–9429, https://doi.org/10.1002/adma.201602776.

[44] L. Zhan, S. Li, T.-K. Lau, Y. Cui, X. Lu, M. Shi, C.-Z. Li, H. Li, J. Hou, H. Chen, Over 17% efficiency ternary organic solar cells enabled by two non-fullerene acceptors working in an alloy-like model, Energy Environ. Sci. 13 (2020) 635–645, https://doi.org/10.1039/C9EE03710A.

[45] D. Wang, F. Zhang, M. Li, Y. Liu, A. Geng, J. Zhou, X. Li, D. Xu, Optimization light utilization efficiency of semitransparent organic solar cells by regulating absorption spectrum, ACS Appl. Energy Mater. 7 (2024) 6013–6020, https://doi.org/10.1021/acsaem.4c01498.

[46] Z. Wang, Z. Peng, Z. Xiao, D. Seyitliyev, K. Gundogdu, L. Ding, H. Ade, Thermodynamic properties and molecular packing explain performance and processing procedures of three D18:NFA organic solar cells, Adv. Mater. 32 (2020) 2005386, https://doi.org/10.1002/adma.202005386.

[47] Y. Song, K. Zhang, S. Dong, R. Xia, F. Huang, Y. Cao, Semitransparent organic solar cells enabled by a sequentially deposited bilayer structure, ACS Appl. Mater. Interfaces 12 (2020) 18473–18481, https://doi.org/10.1021/acsami.0c00396.

[48] J. Oh, J.H. Kim, Y.R. Kim, A. Armin, S. Lee, K. Park, H. Kang, K. Lee, Photopically transparent organic solar cells with tungsten oxide-based multilayer electrodes, ACS Appl. Mater. Interfaces 15 (2023) 42802–42810, https://doi.org/10.1021/acsami.3c08028.

[49] J.W. Yoon, H. Bae, J. Yang, J.-W. Ha, C. Lee, J. Lee, S.C. Yoon, H. Choi, S.-J. Ko, Semitransparent organic solar cells with light utilization efficiency of 4% using fused-cyclopentadithiophene based near-infrared polymer donor, Chem. Eng. J. 452 (2023) 139423, https://doi.org/10.1016/j.cej.2022.139423.

[50] Y. Zhang, W. Deng, C.E. Petoukhoff, X. Xia, Y. Lang, H. Xia, H. Tang, H. T. Chandran, S. Mahadevan, K. Liu, P.W.K. Fong, Y. Luo, J. Wu, S.-W. Tsang, F. Laquai, H. Wu, X. Lu, Y. Yang, G. Li, Achieving 19.4% organic solar cell via an in situ formation of p-i-n structure with built-in interpenetrating network, Joule 8 (2024) 509–526, https://doi.org/10.1016/j.joule.2023.12.009.

[51] B. Liu, O.J. Sandberg, J. Qin, Y. Liu, S. Wilken, N. Wu, X. Yu, J. Fang, Z. Li, R. Huang, W. Zha, Q. Luo, H. Tan, R. Österbacka, C.-Q. Ma, Inverted organic solar cells with an in situ-derived SiOxNy passivation layer and power conversion efficiency exceeding 18%, Nat. Photonics 19 (2025) 195–203, https://doi.org/10.1038/s41566-024-01574-0.